Ceramics International xxx (xxxx) xxx

Contents lists available at ScienceDirect

Ceramics International

journal homepage: www.elsevier.com/locate/ceramint

β-$Ca_3(PO_4)_2$- $Ca_{9.95}Li_{1.05}(PO_4)_7$ lamellar microstructure by chemical etching: Synthesis, characterization and *in vitro* bioactivity

M. Angélica Barbudo [a,*], Pablo Velásquez [a], Ángel Murciano [b], Piedad N. De Aza [a]

[a] Instituto de Bioingeniería, Universidad Miguel Hernández, Avda. Universidad S/n, Elche, Alicante, 03202, Spain
[b] Departamento de Materiales, Óptica y Tecnología Electrónica, Universidad Miguel Hernández, Avda. Universidad S/n, Elche, Alicante, 03202, Spain

ARTICLE INFO

Keywords:
A. sol-gel process
B. microstructure-final
D. Apatite
E. Biomedical applications

ABSTRACT

In this study, new multilayer 3D porous scaffolds were designed with a core composed of Ca_3O_5Si (C_3S) and external layers composed of $Ca_5Li_2(PO_4)_4$. Scaffolds' surface topography was modified to reveal a lamellar microstructure by applying chemical etching. Scaffolds were characterized by X-Ray Diffraction (XRD), Field Emission Scanning Electron Microscopy with Energy Dispersive X-ray spectroscopy (FESEM/EDX), Fourier Transform Infrared Spectroscopy (FTIR) and Mercury Porosimetry. *In vitro* bioactivity was evaluated by immersing scaffolds in simulated body fluid (SBF) at 1, 3 and 7 days. Scaffolds presented calcium pyrophosphate, β-tricalcium phosphate (β-TCP), nonstoichiometric and stoichiometric calcium/lithium phosphate as the main phases. The calcium pyrophosphate and stoichiometric calcium/lithium phosphate in the external layer were eliminated by the chemical etching process, which revealed the lamellar microstructure. Lamellar width varied from 1.44 μm to 0.73 μm depending on the chemical etching time. The obtained mechanical strength results influenced samples' macroporosity, which ranged from 50 % to 64 %. These samples also exhibited microporosity between 30.3 % and 49.0 %. During the bioactivity test, all the chemically etched samples showed a hydroxyapatite-like (HA-like) precipitate, except for the sample chemically etched for 30 s at day 1. At day 7, the lamellar microstructure in the samples chemically etched for 30 s and 45 s (C-30 s and C-45 s) was completely covered by the HA-like precipitate, whereas the lamellar microstructure in the sample chemically etched for 60 s (C-60 s) was only partially covered by the HA-like precipitate.

1. Introduction

Nowadays, population aging, sedentary lifestyles, trauma and various bone diseases, including periodontitis, that require bone repair or regeneration are challenging researchers [1]. To solve the above-described problems, new biomaterials with optimal and specific properties are being developed to improve the population's quality of life, and are innovating around personalized medicine and tissue engineering [1,2].

In this context, tissue engineering focuses on developing synthetic implants for bone regeneration that should be bioactive and biodegradable, and capable of promoting osseointegration and osteoinduction [1,3–6]. The development of bone substitutes also requires the creation of porous materials that enhance bioresorption and improve bioactivity, and the porosity of these materials must be interconnected to facilitate bone growth.

In addition to the previously mentioned characteristics, it has been demonstrated that surface morphology plays a decisive role in cell behavior by modifying the parameters of adhesion, proliferation and differentiation, which strongly impact bone formation [4–8]. Moreover, surface topography plays an important role in cell alignment, elongation and migration [9], and lamellar structure modulates cell-cell communication [10].

Currently, there are several chemical techniques, including plasma surface, chemical crosslinking and polymer demixing, and physical techniques like electrospinning, photolithography and electron beam lithography, that attempt to modify developed materials' surface. However, these techniques have some disadvantages. For example, chemical techniques can be toxic and induce cell death due to solvents use, and physical techniques are oriented mainly to flat surfaces [7,11].

Another methodology to modify surface topography is chemical etching, which is a simple and economical technique [7]. To successfully apply this technique, it is necessary to develop specific formulations that feature surface phases with varying dissolution rates compared to the

* Corresponding author. Instituto de Bioingeniería Universidad Miguel Hernández, 03202, Elche, Alicante, Spain.
E-mail addresses: mbarbudo@umh.es (M.A. Barbudo), pavelasquez@umh.es (P. Velásquez), amurciano@umh.es (Á. Murciano), piedad@umh.es (P.N. De Aza).

https://doi.org/10.1016/j.ceramint.2024.10.220
Received 30 July 2024; Received in revised form 8 October 2024; Accepted 14 October 2024
Available online 16 October 2024

applied dissolution conditions. In this regard, multilayer scaffolds are currently being developed to tailor the behavior of structures for specific applications. These scaffolds enable the design of layers based on set objectives. The core can be designed to replicate the porous bone structure, while external layers can provide mechanical strength and incorporate phases of interest. These scaffolds' surface topography can be modified by applying chemical etching techniques to enhance tissue integration.

This work aims to develop a porous 3D material based on a multilayer structure consisting of the following layers: a core formed by tricalcium silicate (C_3S) and external layers according to the $Ca_5Li_2(PO_4)_4$ formulation, where lithium ions (Li^+) partially replace the calcium ions (Ca^{2+}) in the $Ca_3(PO)_2$ formulation. Li^+ is an important element that has significant positive effects on organisms, such as improving osteogenesis to form bone tissue, and also the incorporation of Li+, and other ions like Na^+, Mg^{2+} and K^+, in scaffolds is a method that improves bone regeneration at low cost [12–14].

2. Materials and methods

2.1. Materials preparation

Ceramic scaffolds were prepared by the sol-gel method in combination with the polymeric sponge replication method [15,16]. The preparation process was divided into stage 1 (core preparation) and stage 2 (external layers) (see Table 1). The core preparation formulation was C_3S, which was prepared with 10.5 mL of $Si(OC_2H_4)_4$ (TEOS, Aldrich-Tetraethyl Orthosilicate), 5 mL of ethanol 97°, 5 mL of distilled water and 1 mL of hydrochloric acid (HCl 37 %, Ensure). The mixture was stirred for 10 min to promote the hydrolysis reaction. Simultaneously, a solution of 14.1 g of calcium carbonate ($CaCO_3$, Sigma), 15 mL of distilled water and 15 mL of hydrochloric acid (HCl 37 %, Ensure) was prepared and added to the previous solution. The pH of the final solution was adjusted to between 2 and 3 by adding HCl drop by drop.

Subsequently, polyurethane sponges were cut into cylindrical shapes (20 ppi, 12.7 mm diameter, 10 mm high), submerged in sol-gel solution and oven-dried at 175 °C for 10 min once the first layer had dried. This process was repeated about 15 times until sponge bridges were completely covered. Then sponges were sintered in a furnace at 1050 °C at a heating rate of 18.5 °C/h. This temperature was maintained for 8 h and cooled to room temperature inside the oven.

Once the initial scaffold, called the core, was obtained, it was covered with external layers. The core coatings formulation $Ca_5Li_2(PO_4)_4$ was prepared by mixing 11.5 mL of $(C_2H_4)_3PO_4$ (TEP, Aldrich-Trietyl Phosphate), 5 mL of ethanol 97°, 20 mL of distilled water, 15 mL of hydrochloric acid (HCl 37 %, Ensure), 8.42 g of calcium carbonate ($CaCO_3$, Sigma) and 1.24 of lithium carbonate (Li_2CO_3, Scharlau). The pH of the solution was adjusted to between 2 and 3 by adding HCl drop by drop.

With the previously described solutions, the core was coated and dried at 190 °C for 15 min. This process was repeated 3 times to not eliminate core scaffold porosity. Finally, scaffolds were sintered at a heating rate of 115 °C/h, the final temperature of 1050 °C was reached and maintained for 4 h, and cooled to room temperature inside the furnace. The process was repeated 3 times.

Table 1
Reagents used in the preparation of cores and external coating.[a]

Formulation composition	$CaCO_3$ (g)	Li_2CO_3 (g)	Triethyl phosphate TEP (mL)	Tetraethyl orthosilicate TEOS (mL)
Ca_3SiO_5	14.1	–	–	10.5
$Ca_5Li_2(PO_4)_4$	8.42	1.24	11.5	–

[a] All the preparations were carried out with 20 mL of distilled water, 15 mL of HCl and 5 mL of ethanol to obtain 10 g of formulation.

2.2. Material characterization

The mineralogical composition of the powder material was determined by X- Ray Diffraction (XRD) in a Bruker-AXR D8 Advance using Cu-Kα radiation (1.541874 Å). Data were collected in the Bragg-Brentano theta-2theta (θ/2θ) geometry between 10° and 55° (2θ) in 0.05 steps by counting 5 s per step. The X-ray tube was operated at 40 kV and 30 mA. The obtained diffractograms were analyzed by version 3.16 of the Match! 3 software. The semiquantitative analysis of the phases in scaffolds was carried out following the Relative Intensity Ratio method (RIR), and phases and were compared to the Crystallography Open Database (COD).

Multilayer ceramic scaffolds' morphology was characterized by Field Emission Scanning Electron Microscopy with Energy Dispersive X-ray spectroscopy (FESEM/EDX) using a SIGMA 300 VP of Zeiss with Zeiss SmartEDX. All the samples were palladium-coated before being analyzed.

Chemical composition was evaluated by Fourier Transform Infrared Spectroscopy (FTIR, spectrometer 4700 IRT 5200 Jasco equipped with an ATR PRO ONE accessory). Spectra were collected between 500 cm^{-1} and 1250 cm^{-1} with 16 accumulations, and at a resolution of 4 cm^{-1} and a scanning speed of auto 2 mm/s.

Scaffolds' porosity and pore size (<300 μm) distribution were determined by the Mercury Porosimetry Technique (Poremaster 60 GT Quantachrome instruments) within a pressure range between 1.055 psi and 35216.264 psi. Porosity associated with pore size exceeding 300 μm was determined followed by the application of Archimedes' Principle in mercury.

Scaffolds' mechanical strength was evaluated by a compression test using a Simple Manual Test Stand (SVL-1000N, IMADA). Load was manually applied to scaffolds (10 mm diameter, 9 mm high) until the scaffold completely broke. Ceramic scaffolds' compressive strength was calculated from the results of 5 per batch.

2.3. Surface topography and characterization

Ceramic scaffolds' surface was modified by the selective removal of the more acid-soluble phases by a chemical etching process. An etching solution was prepared by dissolving acetic acid glacial (CH_3COOH, PanReac) in distilled water with stirring to ensure complete chemical dissolution at the 3 % concentration. Scaffolds were submerged in etching solution with stirring to ensure that the whole surface was etched. Finally, scaffolds were rinsed with distilled water to remove any residual etching solution and dried at 80 °C for 24 h. Etching times (30 s, 45 s and 60 s) were tested following the same above-described procedure. The whole process was conducted at room temperature. The modified scaffolds were characterized by FESEM/EDX and XRD.

2.4. In vitro bioactivity characterization

In order to evaluate the chemical etching effect on patterned scaffolds' *in vitro* bioactivity, bioactivity tests were performed by immersion in simulated body fluid (SBF) according to the procedure established by Kokubo et al. [17] and following ISO 23317:2014. The specimens in SBF were incubated in a water bath at 37 °C for 1, 3, and 7 days. After each period, scaffolds were dried at 80 °C for 24 h and analyzed by FESEM/EDX. Variations in the calcium (Ca^{2+}), lithium (Li^+), silicon (Si^{4+}) and phosphorus (P^{5+}) ion concentrations were determined by Inductively Coupled Plasma Optical Emission Spectrometry (ICP-OES Thermo iCAP 6500 DUO).

3. Results

3.1. Scaffolds characterization

Fig. 1 shows the diffraction patterns of the core coating, samples

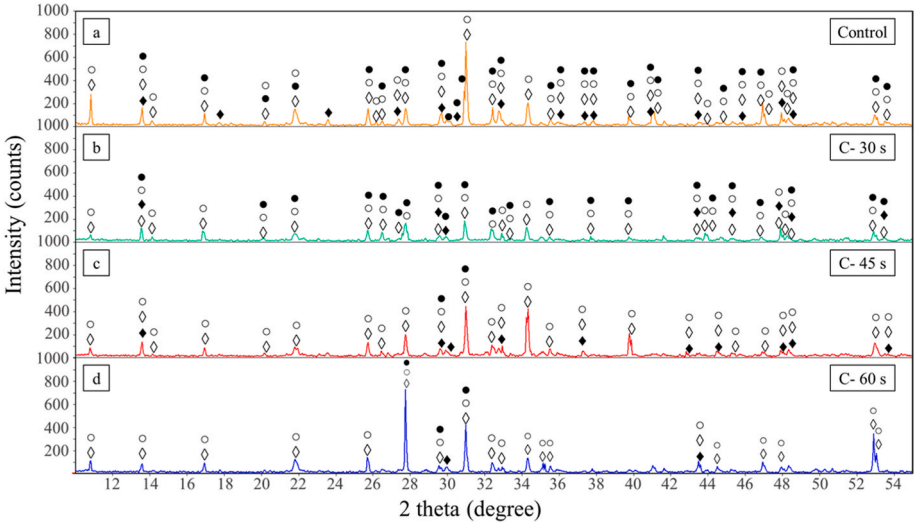

Fig. 1. XRD patterns of the multilayer scaffolds (a) before chemical etching and (b), (c) (d) after the 30 s, 45 s and 60 s chemical etching, respectively. (Main phases: • $Ca_2P_2O_7$, ○ β-$Ca_3(PO_4)_2$, ◊ $Ca_{9,95}Li_{1,05}(PO_4)_7$, ◆ $CaLi(PO_4)$).

before chemical etching (control) and after chemical etching (C-30 s, C-45 s and C-60 s). The XRD pattern of the control showed characteristic peaks of the main phases: calcium pyrophosphate ($Ca_2P_2O_7$) (COD: 96-100-1557), β-tricalcium phosphate (β-TCP) (β-$Ca_3(PO_4)_2$) (COD: 96-151-7239), nonstoichiometric and stoichiometric calcium/lithium phosphate ($Ca_{9,95}Li_{1,05}(PO_4)_7$) (COD: 96-152-6054) and ($CaLi(PO_4)$) (COD: 96-152-6054), considering the rest as minority phases. Table 2 shows the percentage of present phases.

Furthermore, the diffraction patterns of samples C-30 s, C-45 s and C-60 s showed the same phases as the control (Fig. 1). As the chemical etching time increased, a decrease in the calcium pyrophosphate ($Ca_2P_2O_7$) and ($CaLi(PO_4)$) phases (COD: 96-152-6054) was observed, with values of 3 % and 1 %, respectively, in the most chemically etched C-60 s sample (Table 2).

Fig. 2 shows the multilayer ceramic scaffolds analyzed by FESEM/EDX. The control (a) displays hexagonal grains (•) of Ca and P, where the Ca/P ratio varies from the edge to the center of these grains. In the center of the hexagonal grains, the Ca/P ratio is 1.3 and 1.2 on the edge. Equiaxial grains (◘) with a Ca/P ratio of 1.5 and rods (→) with a ratio of 1.0 were also observed in the microstructure. The samples C-30 s, C-45 s and C-60 s showed that some equiaxial grains (◘) remaineds, with a new lamellar structure (▲) after chemical etching. These lamellar structures observed on samples after chemical etching had a Ca/P ratio of 1.4.

Fig. 3 window depicts a representative scaffold of all the samples employed for the Mercury Porosimetry, which exhibits interconnected open porosity that could favor uniform cell seeding, nutrient and metabolite diffusion [18,19]. Table 3 presents porosity, compressive strength and lamellar width, obtained by the control, and samples C-30 s, C-45 s and C-60 s Fig. 3 (a) shows how two regions of volume intruded describe the control sample. The first region reveals how the intruded mercury volume increased from 0 to 0.1252 cc/g, and corresponded to a range of pore diameters between 215 μm and 4.8 μm, respectively. In contrast, the second region displays a slightly intruded mercury after 4.8 μm of pore diameter. Fig. 3 (b) depicts how the control presented four pore peaks corresponding to 124.8 μm, 20.8 μm, 8.1 μm and 6.3 μm. The control presents a mercury porosity of 30.3 % (<300 μm) and Arquimedes porosity of 50 % (>300 μm).

For samples C-60 s and C-30 s, Fig. 3 (a) shows two regions of volume intruded on both curves; the first region with an increased intruded mercury volume from 0 to 0.1585 cc/g and 0.1732 cc/g, respectively, within the range of pore diameters 215 μm and 4.8 μm. Additionally, C-45 s scaffolds presented a bigger intruded mercury volume than the control and samples C-30 s and C-60 s, from 0 to 0.2757 cc/g, which was almost double the volume intruded within a similar range of pore diameters.

In Fig. 3 (b), C-30 s samples have four pore diameter peaks at 80.0 μm, 8.1 μm, 6.3 μm and 4.9 μm. These samples present mercury porosity of 36.0 % (<300 μm) and Arquimedes porosity of 59 % (>300 μm). The C-45 s samples have the four biggest pore diameter peaks at 46.6 μm, 14.0 μm, 8.1 μm and 4.9 μm, with mercury porosity of 49.0 % and Arquimedes porosity of 62 % (>300 μm).

Finally in Fig. 3 (b), C-60 s samples show two of the biggest diameter peaks at 124.8 μm and 40.9 μm. For these samples, mercury porosity was 38.5 % (<300 μm) and Archimedes porosity of 64 % (>300 μm).

Regarding mechanical properties, the compressive strength of the different samples was between 0.5 ± 0.1 MPa and 0.7 ± 0.1 MPa. While the width lamellar showed a decreased behavior in the function of the etched chemical times (C-30 s, C-45 s and C-60 s) of 1.44 μm, 0.8 μm and 0.73 μm, respectively.

Fig. 4 shows the FTIR spectra of the control sample, while Table 4 presents the vibration modes assigned to each observed signal band. Within the spectrum, the signal observed at 1115 cm^{-1} corresponded to the Si-O-Si asymmetrical stretching, which has been reported between 1000 and 1300 cm^{-1} [20–22]. Although the signals between 1081 cm^{-1} and 1005 cm^{-1} correspond to the overlap of the asymmetrical stretching of groups Si-O-Si and PO_4^{3-}, the last one usually presents a vibrational mode of 1000–1100 cm^{-1} [20]. The signals observed at between 902 cm^{-1} and 970 cm^{-1}, and those at 542 cm^{-1} and 603 cm^{-1}, correspond to the symmetrical stretching and bending stretching PO_4^{3-} reported at 900-970 cm^{-1} [20] and 520-660 cm^{-1} [3,20,21], respectively. The presence of Si-O-Si is corroborated by 793 cm^{-1}, and corresponds to symmetrical stretching or bending vibrations reported between 760 cm^{-1} and 850 cm^{-1} [20–22].

Table 2
RIR analysis of the phases in scaffolds.

Sample/ %	$Ca_2P_2O_7$	β-TCP	$Ca_{9,95}Li_{1,05}(PO_4)_7$	CaLi (PO_4)	Minority phases
Control	19	44	16	10	11
C-30 s	18	56	12	4	10
C-45 s	1	41	44	5	9
C-60 s	3	33	49	1	14

3.2. *In vitro* bioactivity

In relation to *in vitro* bioactivity, scaffolds were tested by soaking

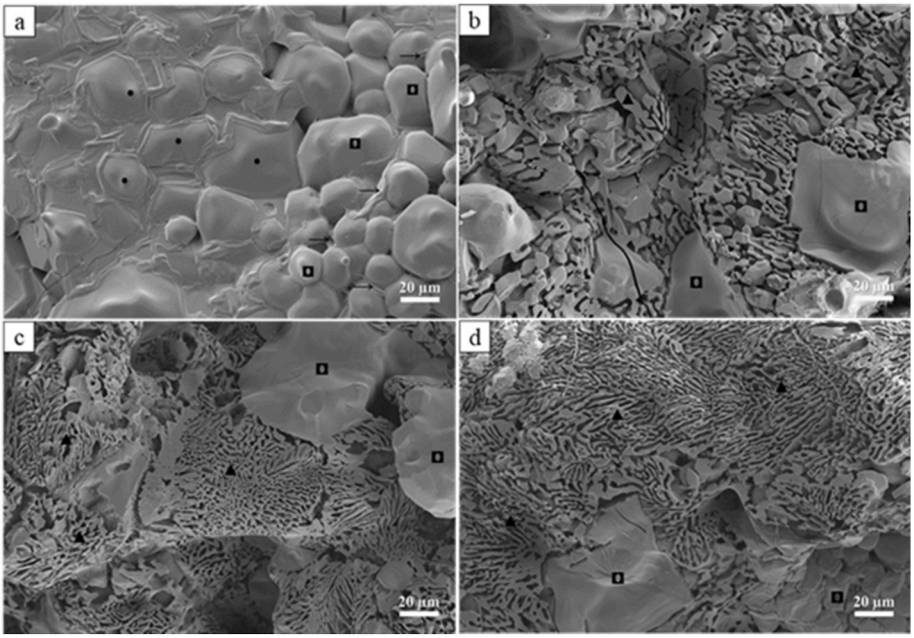

Fig. 2. FESEM micrographs of the scaffold surface: (a) control, (b) C- 30 s, (c) C- 45 s and (d) C- 60 s.

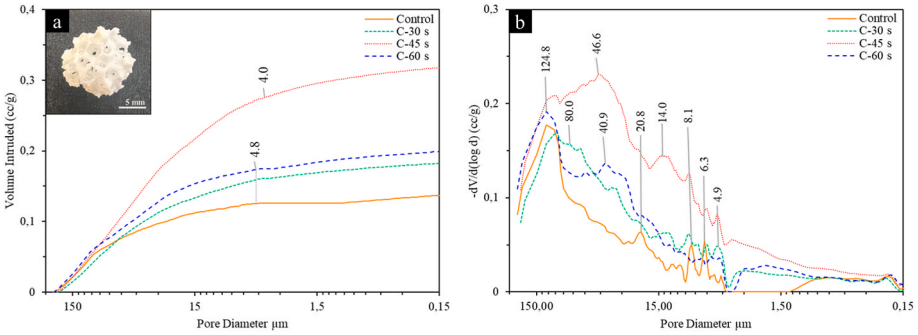

Fig. 3. Representative optical image of scaffolds (window). Mercury Porosimetry curves: (a) Cumulative and (b) Differential intrusion vs. pore diameter in scaffolds.

Table 3
Summary of the porosity, compressive strength and width lamellar of the control, C-30 s, C-45 s and C-60 s scaffolds.

Sample	Porosity <300 µm[a]	Porosity >300 µm[b]	Compressive strength	Lamellar width
	(%)		MPa	µm
Control	30.3	50 ± 1	0.6 ± 0.1	–
C-30 s	36.0	59 ± 2	0.6 ± 0.1	1.44 ± 0.04
C-45 s	49.0	62 ± 2	0.7 ± 0.1	0.8 ± 0.2
C-60 s	38.5	64 ± 2	0.5 ± 0.1	0.73 ± 0.08

[c] Simple Manual Test Stand.
[a] Obtained by the Mercury Porosimetry Technique.
[b] Obtained by Archimedes Principle in mercury.

them in SBF solution for 1, 3 and 7 days. The control scaffolds did not show any HA-like precipitate or significant change on the surface during the test (Fig. 5a–e and i).

Fig. 5(b–f and j) depicts C-30 s samples after SBF immersion at 1, 3 and 7 days, respectively. After immersion, the sample still presented hexagonal grain and lamellar structure, observed before being soaked in SBF (Fig. 2 (b)). At 1 day, no HA precipitate was observed on scaffolds. However, from day 3 to day 7, samples were partially covered by a HA-like precipitate with a Ca/P ratio of 1.44.

Fig. 5(c–g and k) also shows the C-45 s scaffold surface after SBF

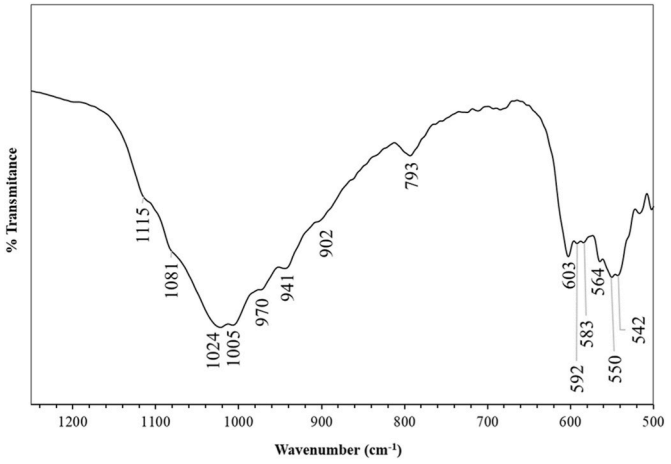

Fig. 4. The scaffold FTIR spectra. The Control Sample.

immersion at 1, 3 and 7 days. Samples presented a Ca-P precipitate with globular morphology on the surface. The EDX indicated variation in the Ca/P ratio from 1.45 at 1 day, to a Ca/P ratio of 1.65 at day 7, which corresponds to carbohydroxyapatite. The Ca/P ratio value was slightly

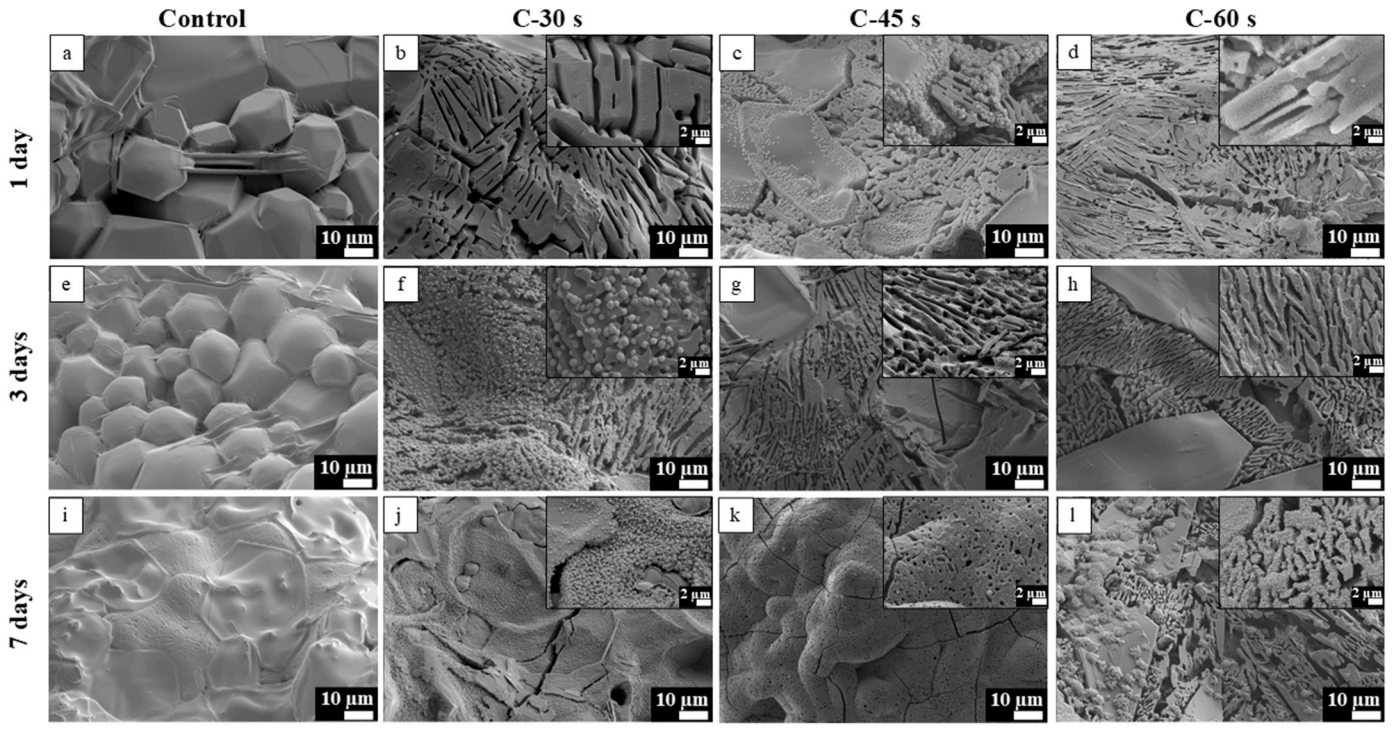

Fig. 5. FESEM images obtained after the *in vitro* bioactivity evaluation of the control scaffolds and the chemically etched scaffolds (C-30 s, C-45 s and C-60 s) at days 1, 3 and 7.

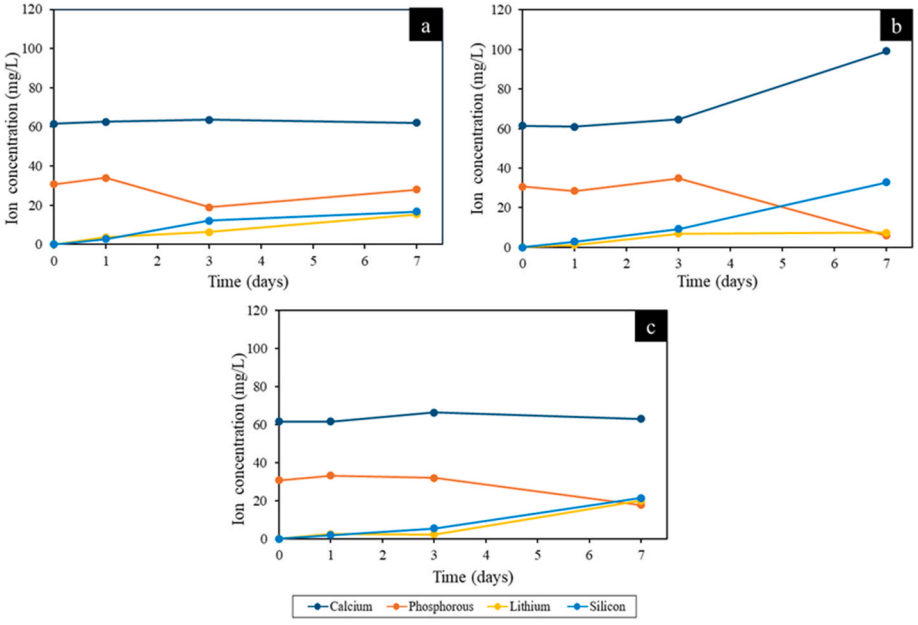

Fig. 6. The ion concentration in SBF at different times after soaking scaffolds: (a) C-30 s, (b) C-45 s and (c) C-60 s.

Table 4
The scaffold FTIR vibrational modes.

Wavenumber (cm^{-1})	Vibrations	References
1115/1081/1024/1005	Si-O-Si asymmetrical stretching	[20,22]
1081/1024/1005	PO_4^{3-} asymmetrical stretching	[20]
970/941/902	PO_4^{3-} symmetrical stretching	[20]
793	Si-O-Si symmetrical stretching or bending	[20,22]
603/592/583/564/550/542	PO_4^{3-} bending stretching	[3,20,21]

lower than the stoichiometric HA. At that time the surface was completely covered with a HA-like precipitate layer.

Finally, Fig. 5(d–h and l) presents C-60s scaffold after SBF immersion at 1, 3 and 7 days, respectively. The sample shows the same morphology on the surface as in Fig. 2 (d), but was partially covered by a Ca-P precipitate from day 1 to day 7. EDX revealed variation in the ratio Ca/P from 1.40 to 1.52.

EDX also showed other ions, such as Na^{+} and Mg^{2+}, present in SBF, which could change the Ca/P ratio.

To evaluate *in vitro* bioactivity, the changes in the Ca^{2+}, Li^{+}, Si^{4+} and

P^{5+} concentrations in SBF were measured by ICP-OES. Fig. 6 shows the data obtained after immersion in SBF for each C-30 s, C-45 s and C-60 s sample at different times.

The ionic behavior of C-30 s samples in SBF (Fig. 6 (a)) showed that the: (i) calcium concentration generally remained constant from day 1 to day 7; (ii) phosphorus concentration slightly lowered until day 3 and then slightly increased to day 7; (iii) the lithium and silicon concentrations, whose initial concentrations were zero, progressively increased during the assay.

The curve of C-45s samples (Fig. 6 (b)) showed that: (i) the calcium concentration remained almost constant from day 1 to day 3 because at this time, this concentration significantly increased to day 7; (ii) at 7 days, the concentrations of the phosphorus and silicon ions displayed specular behavior, while the silicon ions were released and the phosphorus ions were adsorbed by the scaffold; (iii) lithium, whose initial concentration was zero, increased to day 7 days and Li^+ ions were released from scaffolds.

Fig. 6 (c) shows the ionic behavior curve of C-60 s samples in the SBF: (i) the concentrations of the calcium and lithium ions were similar to those of C-30 s; (ii) the concentrations of the phosphorus and silicon ions remained almost constant until day 3. Then the concentration of the silicon ions increased, but the concentration of the phosphorus ions decreased to day 7.

4. Discussion

In this study, new 3D porous ceramic scaffolds were developed by the sol-gel and polymer sponge replica methods as described by other authors [7,15]. These combined methods allow interconnected pores and large surface area scaffolds to be obtained for tissue engineering [16]. The new multilayer scaffolds consisted of a core with a C_3S composition, which was coated with $Ca_5Li_2(PO_4)_4$ external layers. After sintering, the following phases were obtained in the control: β-TCP, $Ca_{9.95}Li_{1.05}(PO_4)_7$, $Ca_2P_2O_7$, $CaLi(PO_4)$, C_2S, CS and SiO_2.

The formation of these phases depends on the presence of the Li^+ on the external layers. As Li^+ is a monovalent ion with a smaller radius than Ca^{2+} (Ca^{2+}: 1.04 Å; Li^+: 0.68 Å) [23], it generates stress when incorporated into the crystal lattice of phosphate groups. This stress leads to the formation of the most stable phases based on the calcium and phosphate groups present. TCP is known to be a highly stable phase when there is high calcium content. As the external layer was formulated from TCP with the Ca^{2+} substituted by the Li^+, the composition was deficient in Ca^{2+}, which was why the phases with a Ca/P ratio lower than 1.5 were also obtained, which was the case of $CaLiPO_4$ and the iso-structural of β-TCP ($Ca_{9.95}Li_{1.05}(PO_4)_7$). Other researchers, such as C. Q. Zhao et al. and O. Kaygili et al., have successfully synthesized structures with similar phases, but the resulting microstructures differed. This variation may be attributed to multilayer composition, differences in the sintering temperatures of lithium calcium phosphates, fabrication processes and lack of chemical etching, which highlights the novelty of the proposed scaffolds [24–26].

Additionally, SiO_2 is derived from C_3S, which suggests that the initially formulated C_3S acts as an additional source of calcium. The main phosphate phases interact to form the lamellar structure revealed by chemical etching. This lamellar structure consists of β-TCP and $Ca_{9.95}Li_{1.05}(PO_4)_7$, while the $Ca_2P_7O_2$ and $CaLi(PO_4)$ phases are removed in varying proportions depending on the chemical etching time (Table 2). Sebastian et al. investigated scaffolds with a composition of $2SiO_2$-50CaO-$48P_2O_5$ and observed a similar structure characterized by ridges and grooves. By varying chemical etching times and solution concentrations, they achieved the dissolution of the calcium pyrophosphate phase. However, the modification of the ridge widths in the microstructure was limited [7]. In our study, apart from dissolving the calcium pyrophosphate phase, the results indicated that chemical etching also dissolved $CaLiPO_4$. This behavior arises because the β-TCP phase, and its isostructural phases, exhibit a lower dissolution rate at acid pH compared to other calcium phosphate phases. Generally, as the Ca/P ratio decreases, the dissolution rate of the phases increases [27–29]. The dissolution of this phase allowed the better modulation of lamellae widths.

The degree of dissolution of phases was determined by the chemical etching time, with the peaks of the $Ca_2P_7O_2$ and $CaLiPO_4$ phases generally tending to decrease in the diffractogram of XRD (Fig. 1). In this way, all the chemically etched samples presented the same phases as the control. However, the peaks corresponding to $Ca_2P_7O_2$ and $CaLiPO_4$ presented less intensity by going from 19 % in the control to 3 % in C-60 s, and from 10 % in the control to 1 % in C-60 s, respectively (Table 2). In C-45 s samples and C-60 s, the $Ca_2P_7O_2$ phase was almost completely eliminated due to the dissolution of this phase in the 3 % CH_3COOH solution. Depending on the immersion time, the dissolution of these phases revealed the lamellar microstructure, which modified lamellar width and porosity <300 μm.

The FESEM study of the control scaffolds' surface microstructure revealed the presence of calcium pyrophosphate and β-TCP phases (Fig. 2 (a)). The tricalcium phosphate phase often shows a hexagonal grain with a Ca/P ratio of 1.5 [30]. This study also allowed the observation of a rod structure with a Ca/P ratio of 1, which corresponded to the calcium pyrophosphate phase. Another grain type was also observed by FESEM and it presented a different Ca/P ratio from the center to the edges: 1.3 to 1.2, respectively. This could mean that the grain was not stoichiometric β-TCP, but a combination of phosphate phases.

Morphologically similar lamellar structures, albeit with different phases, have been observed in other studies [7]. However, the structures obtained in this study, modulated with a lower concentration of chemical etching solution and shorter immersion times, indicated a higher dissolution rate of the involved phases.

One of the most important factors in designing the scaffold is the porosity because the control of this feature, macroporosity (pore size >100 μm) and microporosity (pore size <10 μm), allows the development of important cellular processes to promote bone growth and optimal ionic exchange [31–33].

Fig. 3 shows that the control scaffolds had four significant averages of different pore sizes, over 124.8 μm, 20.8 μm, 8.1 μm and 6.3 μm, and this porosity was also observed between the grains in the image corresponding to the control microstructure. These scaffolds also presented porosity <300 μm of 30.3 %, but the resulting porosity was 50 % at the macrolevel (>300 μm).

Once scaffolds had been chemically etched, pore size averages were also modified. The C-30 s scaffolds had higher pore size averages, with 80.0 μm, 8.1 μm and 4.9 μm, while C-45 s showed relevant data of 46.6 μm, 14 μm and 4.9 μm. Finally, C-60 s scaffolds obtain average pore size distributions of 124.8 μm and 40.9 μm.

The elimination of the $Ca_2P_2O_7$ and $CaLi(PO_4)$ phases generally led to an increase in both macro- (>300 μm) and micro- (<300 μm) porosities. In line with this, previous studies have demonstrated that porosity above 50 μm has beneficial effects on osteogenic quality, while porosity below 10 μm creates a large surface area that stimulates ion exchange and bone protein adsorption [34,35].

In this context, we aimed to create a scaffold by simple methods, such as sol-gel and the polymeric sponge technique, which involve different porosity levels that can be adapted to requirements. The obtained porous lamellar structure of β-TCP and $Ca_{9,95}Li_{1,05}(PO_4)_7$ is expected to evolve once implanted because the main bone tissue phase is similar to TCP and has been successfully used when doped with other ions. Thus the scaffolds herein developed can form a hierarchical structure capable of mimicking bone tissue.

These characteristics are extremely relevant because scaffolds are intended to be used for bone regeneration and, thus, for optimal cell growth and development, and it is important to consider these physical characteristics [31].

Despite discrepancies in the literature on the ideal porosity, it is generally accepted that pores smaller than 10 μm promote protein

adsorption, ion exchange and HA-like formation [36]. However, pores of around 100 μm favor the initial adhesion of osteoblasts [37], and pores larger than 300 μm are necessary for promoting new bone formation [37].

Another essential aspect considered in scaffolds design was resistance to compression. The control's compressive strength was 0.6 ± 0.1 MPa. After chemical etching at different times, compressive strength continued to lie within the same range: between 0.5 ± 0.1 MPa and 0.7 ± 0.1 MPa. This finding means that chemical etching did not damage resistance to compression. This phenomenon can be explained by the mechanical process because, when the scaffold is chemically etched, the pyrophosphate phase is removed. However, it revealed a new lamellar microstructure that was distributed in the complete scaffolds. These lamellar structures can stop or deflect the propagation of surface cracks due to induced compressive loading. These compressive strength values for porous scaffolds are consistent with the literature. Indeed Gibson et al. report a compressive strength range of 0.2–4 MPa when relative density was low [38].

4.1. Scaffolds' in vitro characterization

Scaffolds were immersed in SBF to evaluate their ability to show bioactivity. The control scaffolds did not show any HA-like precipitate over the entire study time range, probably due to the presence of the calcium pyrophosphate phase that can inhibit *in vitro* bioactivity [30]. This calcium pyrophosphate can be found in the human body and plays an important role as a regulator of bone mineralization. The calcium pyrophosphate phase has been demonstrated to block calcium from crystallizing with phosphate and to form HA *in vitro,* but not *in vivo* [39]. Pyrophosphate is also considered poorly resorbable and can inhibit osteoclastic resorption [30].

The chemically etched scaffolds' *in vitro* bioactivity was tested by soaking in SBF for 1, 3 and 7 days. As C-30 s samples showed no HA-like precipitate at 1 day (Fig. 5 (b)) due to the short exposure time (30 s, insufficient to eliminate the pyrophosphate phase). At days 3 and 7 (Fig. 5 (f and j)), a globular precipitate on the surface of the hexagonal grain and on the lamellar structure was observed, and the EDX analysis of precipitates revealed that they were composed of Ca and P, with traces of Na and Mg and a Ca/P ratio of 1.44. Their Ca/P ratio was lower than stoichiometric hydroxyapatite (the stoichiometric value of the Ca/P ratio is 1.67 for pure HA) [39,40]. However, biological HA was generally calcium-deficient and Ca^{2+} could also be substitution by other ions like Mg^{2+}, Na^{+}, K^{+}, among others. The substitution of the ions in HA led to changes in characteristics, crystallinity, morphology and solubility, and also in physical, chemical and biological properties [36,40,41].

In the case of the C-45 s samples (Fig. 5(c–g and k)), the HA-like precipitate developed and covered the surface, with a Ca/P ratio from 1.45 at day 1 to one of 1.65 at day 7, which corresponded to the almost stoichiometric HA value. At day 7, the hexagonal grains and lamellar structure were completely covered by the HA-like precipitate. In this case, in Fig. 5 (k), which corresponds to C-45 s at day 7, that the HA-like precipitate showed a thick collapsed layer, which did not allow the surface to be seen.

Furthermore, C-60 s samples (Fig. 5(d–h and l)) displayed a thin layer of the HA-like precipitate at day 1 (Fig. 5 (d)) with a Ca/P ratio of 1. At day 3 however (Fig. 5 (h)), the precipitate grew to day 7 (Fig. 5 (l)), at which time the observed HA-like precipitate slightly covered both the β-TCP grains and lamellar structure, and had a Ca/P ratio of 1.52. EDX showed Mg^{2+} and Na^{+} ions. These ions can replace Ca^{2+} by causing: (i) a lower Ca/P ratio, (ii) decreased crystallinity or (iii) with the Mg^{2+}, an increased extent of synthetic apatites dissolution [40].

The ionic exchange between scaffolds and SBF explained the behavior of the HA-like precipitation. Because of this, the changes in the concentration of the Ca^{2+}, Li^{+}, Si^{4+} and P^{5+} after different immersion days in SBF were analyzed by ICP-OES (Fig. 6). On day 1, C-30 s scaffolds showed no significant changes, but on day 3, the concentration of the P^{5+} concentration lowered, while the Si^{4+}concentration increased. This means that these scaffolds absorbed phosphorous ions and released silicon ions, which allowed HA-like precipitations to start, as observed in the FESEM image (Fig. 5 (f)). Furthermore on testing days, the concentration of the Li^{+} always increased in SBF, which implies that scaffolds gradually released Li^{+}.

At the earlier days, C-60 s samples (Fig. 6 (c)), the concentrations of the Ca^{2+}, Li^{+}, Si^{4+} and P^{5+} did not significantly change. From day 3 to day 7, the concentration of the SBF phosphorus ions lowered, while that of the silicon ions increased, and scaffolds absorbed phosphorus and released silicon to allow the HA-like precipitate to cover the surface. In this case, lithium ions were released to SBF during the assay.

It was also necessary to study the *in vitro* behavior of the cells in contact with scaffolds to evaluate these structures' performance for bone regeneration.

5. Conclusion

A new multilayer ceramic scaffold was developed using a combined sol-gel and polymeric sponge replica technique by incorporating a core of C_3S and external $Ca_5Li_2(PO_4)_4$ layers. Chemical etching at various time intervals successfully created a lamellar surface microstructure with optimal physical properties, including mechanical strength and porosity. The resulting scaffold exhibited both a similar microstructure and macrostructure to the hierarchical trabecular bone structure. Additionally, this method allowed the precise control of the chemical composition of the different scaffold layers.

Calcium pyrophosphate, β-TCP, nonstoichiometric and stoichiometric calcium/lithium phosphate were obtained as the main phases. Chemical etching was performed with 3 % acetic acid solution. This chemical etching process removed the calcium pyrophosphate and stoichiometric lithium calcium phosphate phases, and revealed the lamellar microstructure constituted by β-TCP and nonstoichiometric calcium/lithium phosphate. Lamellar width varied from 1.44 ± 0.04 μm to 0.73 ± 0.08 μm depending on chemical etching times. This chemical etching did not affect compressive strength, but allowed scaffold bioactivity to be modulated. Thus all the scaffolds showed bioactivity with HA-like precipitation for 3 and 7 days. At day 1, only the scaffolds that were chemically etched for 45 s (C-45 s) and 60 s (C-60 s) showed bioactivity.

The modification of ceramic scaffolds' surface microstructure is an important and promising strategy for improving their *in vivo* osteogenic capacity and improving cell proliferation. It was also possible to modify and modulate scaffolds' lamellar width, which could be used for drug delivery. Finally for a specific aim, cellular and *in vivo* studies are necessary to prove their potential applicability.

CRediT authorship contribution statement

M. Angélica Barbudo: Writing – original draft, Investigation, Formal analysis. **Pablo Velásquez:** Methodology, Formal analysis. **Ángel Murciano:** Writing – original draft, Investigation, Formal analysis. **Piedad N. De Aza:** Validation, Supervision, Funding acquisition, Formal analysis.

Funding

This work is part of Project PID2020-116693RB-C21, funded by MCIN/AEI/10.13039/501100011033 Spain.

Declaration of competing interest

The authors declare that they have no known competing financial interests or personal relationships that could have appeared to influence the work reported in this paper.

Acknowledgments

Ph.D. student M. Angélica Barbudo was funded by a grant from the Government of the Generalitat Valenciana with reference CIGRIS/2022/190.

References

[1] R.G. Ribas, et al., Current advances in bone tissue engineering concerning ceramic and bioglass scaffolds: a review, Ceram. Int. 45 (17) (2019) 21051–21061, https://doi.org/10.1016/j.ceramint.2019.07.096.
[2] M.A. Alghamdi, A.N. Fallica, N. Virzì, P. Kesharwani, V. Pittalà, K. Greish, The promise of nanotechnology in personalized medicine, J. Personalized Med. 12 (5) (2022) 673, https://doi.org/10.3390/jpm12050673.
[3] N. Eliaz, N. Metoki, Calcium phosphate bioceramics: a review of their history, structure, properties, coating technologies and biomedical applications, Materials 10 (4) (2017) 1–104, https://doi.org/10.3390/ma10040334.
[4] A.E. Loiselle, L. Wei, M. Faryad, E.M. Paul, G.S. Lewis, J. Gao, A. Lakhtakia, H. J. Donahue, Specific biomimetic hydroxyapatite nanotopographies enhance osteoblastic differentiation and bone graft osteointegration, Tissue Eng. 19 (2013) 1704–1712, https://doi.org/10.1089/ten.tea.2012.0560.
[5] D. Khang, J. Choi, Y.M. Im, Y.J. Kim, J.H. Jang, S.S. Kang, T.H. Nam, J. Song, J. W. Park, Role of subnano-, nano- and submicron-surface features on osteoblast differentiation of bone marrow mesenchymal stem cells, Biomaterials 33 (26) (2012) 5997–6007, https://doi.org/10.1016/j.biomaterials.2012.05.005.
[6] Y.L. Jung, H.J. Donahue, Cell sensing and response to micro- and nanostructured surfaces produced by chemical and topographic patterning, Tissue Eng. 13 (2007) 1879–1891, https://doi.org/10.1089/ten.2006.0154.
[7] E. Sebastián, A. Murciano, R. Madrigal, P.N. De Aza, P. Velasquez, 3D CaP porous scaffolds with grooved surface topography obtained by the sol-gel method, Ceram. Int. 47 (15) (2021) 21466–21475, https://doi.org/10.1016/j.ceramint.2021.04.158.
[8] D.D. Deligianni, N.D. Katsala, P.G. Koutsoukos, Y.F. Missirlis, Effect of surface roughness of hydroxyapatite on human bone marrow cell adhesion, proliferation, differentiation and detachment strength, Biomaterials (2001) 87–96, https://doi.org/10.1016/s0142-9612(00)00174-5.
[9] S. Lenhert, M.B. Meier, U. Meyer, L. Chi, H.P. Wiesmann, Osteoblast alignment, elongation and migration on grooved polystyrene surfaces patterned by Langmuir-Blodgett lithography, Biomaterials 26 (5) (2005) 563–570, https://doi.org/10.1016/j.biomaterials.2004.02.068.
[10] G. Kirmizidis, M. Res, M.A. Birch, Microfabricated grooved substrates influence cell-cell communication and osteoblast differentiation in vitro, Tissue Eng. 15 (2009) 1427–1436, https://doi.org/10.1089/ten.tea.2008.0137.
[11] R. Teimouri, K. Abnous, S.M. Taghdisi, M. Ramezani, M. Alibolandi, Surface modifications of scaffolds for bone regeneration, J. Mater. Res. Technol. 24 (2023) 7938–7973, https://doi.org/10.1016/j.jmrt.2023.05.076.
[12] N.J. Lakhkar, I.H. Lee, H.W. Kim, V. Salih, I.B. Wall, J.C. Knowles, Bone formation controlled by biologically relevant inorganic ions: role and controlled delivery from phosphate-based glasses, Adv. Drug Deliv. Rev. 65 (4) (2013) 405–420, https://doi.org/10.1016/j.addr.2012.05.015.
[13] N.A. Mata, P. Velasquez, A. Murciano, P.N. De Aza, Multilayer Mg-pyrophosphate glass ceramic with discontinuous bioactivity. Physicochemical characterization, Ceram. Int. 47 (10) (2021) 14612–14620, https://doi.org/10.1016/j.ceramint.2021.02.044.
[14] Diana-Elena Radulescu, Otilia Ruxandra Vasile, Ecaterina Andronescu, Anton Ficai, Latest research of doped hydroxyapatite for bone tissue engineering, Int. J. Mol. Sci. 24 (17) (2023) 13157, https://doi.org/10.3390/ijms241713157.
[15] P. Ros-Tárraga, A. Murciano, P. Mazón, S.A. Gehrke, P.N. De Aza, New 3D stratified Si-Ca-P porous scaffolds obtained by sol-gel and polymer replica method: microstructural, mineralogical and chemical characterization, Ceram. Int. 43 (8) (2017) 6548–6553, https://doi.org/10.1016/j.ceramint.2017.02.081.
[16] P. Ros-Tárraga, Á. Murciano, P. Mazón, S.A. Gehrke, P.N. De Aza, In vitro behaviour of sol-gel interconnected porous scaffolds of doped wollastonite, Ceram. Int. 43 (14) (2017) 11034–11038, https://doi.org/10.1016/j.ceramint.2017.05.146.
[17] T. Kokubo, H. Takadama, How useful is SBF in predicting in vivo bone bioactivity? Biomaterials 27 (15) (2006) 2907–2915, https://doi.org/10.1016/j.biomaterials.2006.01.017.
[18] A.R. Calore, et al., Manufacturing of scaffolds with interconnected internal open porosity and surface roughness, Acta Biomater. 156 (2023) 158–176, https://doi.org/10.1016/j.actbio.2022.07.017.
[19] L. Zhu, D. Luo, Y. Liu, Effect of the nano/microscale structure of biomaterial scaffolds on bone regeneration, Springer Nature (2020) 1–15, https://doi.org/10.1038/s41368-020-0073-y.
[20] H. Aguiar, J. Serra, P. González, B. León, Structural study of sol-gel silicate glasses by IR and Raman spectroscopies, J. Non-Cryst. Solids 355 (8) (2009) 475–480, https://doi.org/10.1016/j.jnoncrysol.2009.01.010.
[21] Y.C. Fredholm, N. Karpukhina, D.S. Brauer, J.R. Jones, R.V. Law, R.G. Hill, Influence of strontium for calcium substitution in bioactive glasses on degradation, ion release and apatite formation, J. R. Soc. Interface 9 (70) (2012) 880–889, https://doi.org/10.1098/rsif.2011.0387.
[22] S. Shahrabi, S. Hesaraki, S. Moemeni, M. Khorami, Structural discrepancies and in vitro nanoapatite formation ability of sol-gel derived glasses doped with different bone stimulator ions, Ceram. Int. 37 (7) (2011) 2737–2746, https://doi.org/10.1016/j.ceramint.2011.04.025.
[23] V.V. Smirnov, et al., Influence of lithium on the structure and phase composition formation in the synthesis of hydroxyapatite, Dokl. Chem. 481 (2) (2018) 177–180, https://doi.org/10.1134/S0012500818080025.
[24] C.Q. Zhao, et al., Doping lithium element to enhance compressive strength of β-TCP scaffolds manufactured by 3D printing for bone tissue engineering, J. Alloys Compd. 814 (2020) 152327, https://doi.org/10.1016/j.jallcom.2019.152327.
[25] O. Kaygili, S. Keser, T. Ates, F. Yakuphanoglu, Synthesis and characterization of lithium calcium phosphate ceramics, Ceram. Int. 39 (7) (2013) 7779–7785, https://doi.org/10.1016/j.ceramint.2013.03.037.
[26] V.A. Morozov, A.A. Belik, R.N. Kotov, et al., Crystal structures of double calcium and alkali metal phosphates Ca10 M(PO4)7 (M = Li, Na, K), Crystallogr. Rep. 45 (2000) 13–20, https://doi.org/10.1134/1.171129.
[27] L. Wang, G.H. Nancollas, Calcium orthophosphates: crystallization and dissolution, Chem. Rev. 108 (11) (2008) 4628–4669, https://doi.org/10.1021/cr0782574.
[28] L.C. Chow, Solubility of calcium phosphates, Monogr. Oral Sci. 18 (2001) 94–111, https://doi.org/10.1159/000061650. PMID: 11758450.
[29] H. Oonishi, H. Oomamiuda, Chapter B8: degradation/resorption in bioactive ceramics in orthopedics, in: J. Black, G. Hastings (Eds.), Handbook of Biomaterial Properties, Chapman and Hall, London, 1998, pp. 406–419.
[30] I.R. Orriss, T.R. Arnett, R.G.G. Russell, Pyrophosphate: a key inhibitor of mineralization, Curr. Opin. Pharmacol. 28 (2016) 57–68, https://doi.org/10.1016/j.coph.2016.03.003.
[31] N. Abbasi, S. Hamlet, R.M. Love, N.T. Nguyen, Porous scaffolds for bone regeneration, J. Sci.: Advance Materials and Devices (2020) 1–9, https://doi.org/10.1016/j.jsamd.2020.01.007.
[32] T.L. Jenkins, D. Little, Synthetic scaffolds for musculoskeletal tissue engineering: cellular responses to fiber parameters, Nature Publishing Group 4 (1) (2019), https://doi.org/10.1038/s41536-019-0076-5.
[33] Z. Tang, X. Li, Y. Tan, H. Fan, X. Zhang, The material and biological characteristics of osteoinductive calcium phosphate ceramics, Regen Biomater 5 (1) (2018) 43–59, https://doi.org/10.1093/rb/rbx024.
[34] L. Morejón, et al., Development, characterization and in vitro biological properties of scaffolds fabricated from calcium phosphate nanoparticles, Int. J. Mol. Sci. 20 (7) (2019), https://doi.org/10.3390/ijms20071790.
[35] P. Diaz-Rodriguez, M. Sánchez, M. Landin, Drug-loaded biomimetic ceramics for tissue engineering, Pharmaceutics 10 (4) (2018) 1–20, https://doi.org/10.3390/pharmaceutics10040272, 272.
[36] D. Xiao, et al., The role of calcium phosphate surface structure in osteogenesis and the mechanisms involved, Acta Biomater. (2020) 22–33, https://doi.org/10.1016/j.actbio.2019.12.034.
[37] Q.L. Loh, C. Choong, Three-dimensional scaffolds for tissue engineering applications: role of porosity and pore size, Tissue Eng. B Rev. 19 (6) (2013) 485–502, https://doi.org/10.1089/ten.teb.2012.0437.
[38] L.J. Gibson, M.F. Ashby, Cellular Solids: Structure and Properties, second ed., Pergamon, Oxford, 1999, pp. 429–452.
[39] M. Canillas, P. Pena, A.H. De Aza, M.A. Rodríguez, Calcium phosphates for biomedical applications, Sociedad Española de Cerámica y Vidrio 53 (2017) 91–112, https://doi.org/10.1016/j.bsecv.2017.05.001.
[40] Donglu Shi, Introduction to Biomaterials, Tsinghua University Press; World Scientific, 2006, pp. 3–12, 13-27, 29-46.
[41] M.L. Dittler, et al., Bioactive glass (45S5)-based 3D scaffolds coated with magnesium and zinc-loaded hydroxyapatite nanoparticles for tissue engineering applications, Colloids Surf. B Biointerfaces 182 (182) (2019) 110346, https://doi.org/10.1016/j.colsurfb.2019.110346.